

# Stormtime ring current heating of the ionosphere and plasmasphere

J. Krall<sup>1</sup>, M.-C. Fok<sup>2</sup>, J. D. Huba<sup>3</sup>, and A. Gloer<sup>2</sup>

<sup>1</sup>Plasma Physics Division, Naval Research Laboratory, Washington, District of Columbia, USA

<sup>2</sup>NASA Goddard Space Flight Center, Greenbelt, Maryland, USA.

<sup>3</sup>Syntek Technologies, Fairfax, Virginia, USA

## Key Points:

- CIMI-computed ring current heating is coupled into SAMI3 to drive a simulation of the stormtime ionosphere and plasmasphere.
- Simulated ring current is shown to directly heat both the plasmasphere and ionosphere.
- A simulation with ring current heating at plasmasphere heights produces elevated stormtime ionosphere temperatures similar to observations.

## Abstract

The energy deposition from ring current ions into the high density ‘cold’ plasma of the ionosphere and plasmasphere is analyzed, based on a Comprehensive Inner Magnetosphere-Ionosphere (CIMI) simulation of the 2015 October 7 storm. In addition, the Naval Research Laboratory (NRL) Sami3 is Also a Model of the Ionosphere (SAMI3) ionosphere/plasmasphere code is used to simulate the effect of ring current heating on the ionosphere and plasmasphere. We find that, during stormtime peaks in the Dst index, energy is deposited at altitudes as low as 100 km. Heating along the entirety of any given field line, both in the ionosphere and plasmasphere, contributes to increased temperatures in the topside ionosphere and inner magnetosphere and to subsequent cold  $O^+$  outflows. However, relative to the heating of the plasmasphere, the direct heating of the ionosphere by ring current ions produces only small effects. Model-data agreement in the  $N^+/O^+$  density ratio shows that these  $O^+$  outflows are driven by thermal forcing.

## Plain Language Summary

When the solar wind encounters Earth’s magnetosphere, a geomagnetic storm can result. These storms generate a ‘ring current’ in the inner magnetosphere. This current, carried by high energy oxygen and hydrogen ions, overlaps with the plasmasphere, a background plasma (mainly hydrogen ions) held in place by Earth’s geomagnetic field. We find that the ring current also overlaps with the near-Earth ionosphere. In previous work, we showed that, when the background plasma is heated by the ring current, oxygen ions flow upward along the geomagnetic field, producing a ‘heavy ion’ population (the  $O^+$  shell) that has been observed. We now focus on the direct heating of the ionosphere by the ring current, versus the indirect effect where energy deposited into the higher altitude plasmasphere is conducted down to the ionosphere by electrons moving along the geomagnetic field. We find that observed stormtime ionosphere temperature increases can be explained by the heat conduction effect. Direct heating of the ionosphere by the ring current does occur during the peak of the storm, but that occurs after the ionosphere is already affected by heat conduction.

## 1 Introduction

Numerical simulations (Fok et al., 1993; Liemohn et al., 2000; Krall et al., 2020; Krall & Huba, 2021) suggest that stormtime ring current heating of plasmasphere and ionosphere electrons (Cole, 1965; R. Comfort, 1996) is a viable mechanism for heating and outflow of  $O^+$  (Roberts et al., 1987; Nosé et al., 2011), subsequent formation of the the  $O^+$  shell, also known as the  $O^+$  torus, and stormtime elevation of ionosphere electron and ion temperatures (Pavlov & Buonsanto, 1997; Liu et al., 2016). By ‘ $O^+$  shell’ we refer a stormtime cold  $O^+$  ion population in the inner magnetosphere. When observed with instrumentation that measures plasmasphere ion composition, the  $O^+$  shell has been found “in the outer plasmasphere” (Chappell, 1982), where it is associated with structured increases in electron temperature (Horwitz et al., 1986, see Fig. 10). When observed via electron and mass density measurements, the  $O^+$  shell is clearly evident outside of the plasmapause, where the average mass clearly exceeds that of the light ions,  $H^+$  and  $He^+$  (Takahashi et al., 2008; Nosé et al., 2011, 2018). Both the plasmasphere and the  $O^+$  shell are cold ion populations in the sense that they are thermal populations with typical ion energies too low to routinely overcome spacecraft charging and be directly detected in situ. Nevertheless, ‘cold’ plasmasphere ion and electron temperatures commonly approach or exceed 1 eV. We use the term  $O^+$  shell (see also Horwitz et al., 1986), because the  $O^+$  density resembles an  $L$ -shell, where  $L$  is the McIlwain parameter (McIlwain, 1961), with  $L$  varying somewhat versus magnetic local time (MLT).

The aim of this study is to further explore the deposition of energy, by ring current ions, into the plasmasphere and ionosphere. We revisit the 2015 October 7 (day 280)

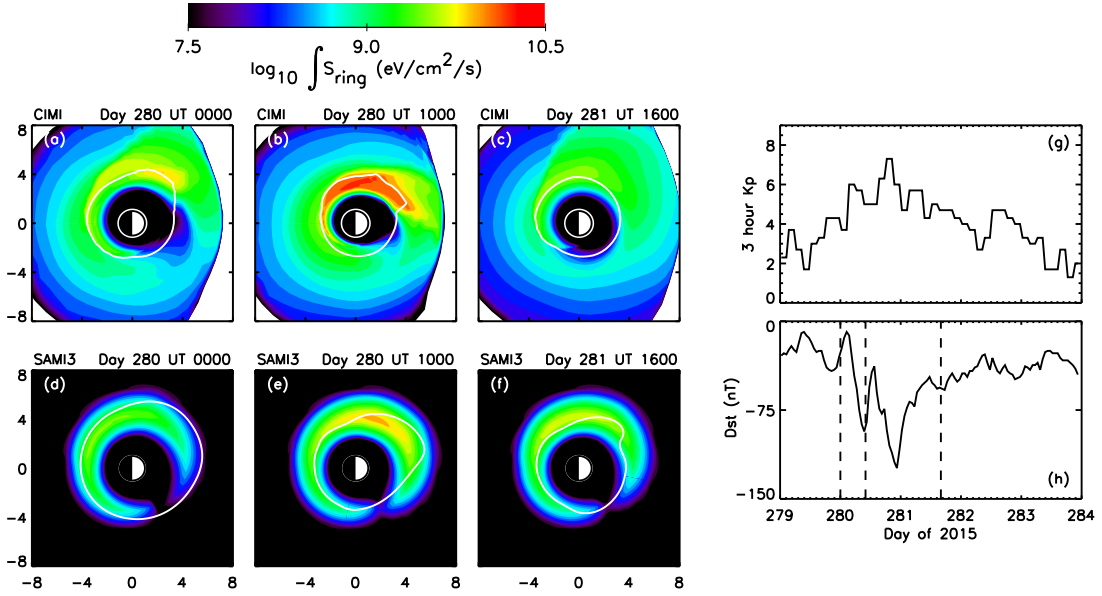


**Figure 1.** (a–c) CIMI model output showing the log of the field-line-integrated electron heating rate, at selected times, plotted as color contours in the magnetic equatorial plane. (d–f) field-line integration of the model ring current heating function of Krall et al. (2020). A single contour line in panels (a–c) and (d–f) indicates plasmasphere electron density  $n_e = 100 \text{ cm}^{-3}$  computed by CIMI or SAMI3, respectively. (g) Kp and (h) Dst geomagnetic indices, which peak on day 280 (7 October) of 2015. Each column corresponds to a time marked by a vertical dashed line in panel (h). The heating rate of panels (a–c) will be used below in the ‘CIMI Heat’ simulation case; panels (d–f) correspond to the ‘Direct Heat’ case.

geomagnetic storm, using the CIMI (Comprehensive Inner Magnetosphere-Ionosphere) model (Fok et al., 2014) to compute ring current heating [see Figure 1(a–c)]. In the next section, we analyze these CIMI calculations to show that the simulated energy losses from the ring current to background electrons includes direct heating of ionosphere electrons by ring current ions via Coulomb collisions. This is followed by simulations, using the SAMI3 (Sami3 is Also a Model of the Ionosphere) ionosphere/plasmasphere model (Huba et al., 2000; Huba & Krall, 2013; Huba et al., 2017). In these simulations we address the effect of the direct heating of the ionosphere by ring current ions and, further, present a simulation in which the CIMI-computed heating rate is interpolated onto the SAMI3 grid. We performed four SAMI3 runs: one with the Krall et al. (2020) model heating function (here the ionosphere is directly heated), one with the model heating applied only at altitudes  $z > R_E/2$ , one with the CIMI-computed heating interpolated to the SAMI3 grid, and one with no ring-current heating. We will refer to these four cases, respectively, as the Direct Heat, Indirect Heat, CIMI Heat, and No Heat cases.

The present study is new in the sense that we visualize, for the first time, the energy deposited by the ring current into both the ionosphere and the plasmasphere. Further, we evaluate the importance, if any, of the direct heating of ionosphere electrons by ring current ions. We further examine the effect of CIMI-computed heating rates on the SAMI3 model ionosphere and plasmasphere. Finally, based on general agreement between simulated and observed  $N^+/O^+$  density ratios, we argue that we have correctly identified a thermal energization mechanism for these heavy ion outflows.

## 2 CIMI modeling of the ring current

The CIMI model (Fok et al., 2014), which is based on the earlier Comprehensive Ring Current Model (Fok et al., 2001; Buzulukova et al., 2010), self-consistently solves the bounce-averaged Boltzmann convection-diffusion equation for ring current particles  $O^+$  and  $H^+$ . The CIMI code computes ring current energy losses via Coulomb collisions between energetic ions and cold background plasmasphere electrons. The CIMI plasmasphere, computed using the dynamic global core plasmasphere model (Ober et al., 1997), is indicated by a white contour line at  $n_e = 100 \text{ cm}^{-3}$  in Figure 1(a–c). These simulations suggest that ring current energy lost to the plasmasphere and ionosphere is a significant effect. It occurs despite the fact that the overlap between the ring current and the plasmasphere is relatively small; the bulk of the ring current lies outside of the plasma-pause (Gringauz, 1983; Kozyra et al., 1997; Burch et al., 2001; Gurgiolo et al., 2005). Because the energy losses are dominated by electron Coulomb collisions (Fok et al., 1995), we focus on this dominant mechanism.

The electron heating from a CIMI simulation of days 279 through 281 of 2015 is shown in Figure 1 (a–c) as contours of the logarithm of the field-line integrated heating rate, plotted in the plane of the magnetic equator and in Figure 2 (a–d) as contours of the logarithm of the heating rate, plotted in a plane of fixed longitude. In Figure 2 (a–d), the CIMI-computed ring current energy loss rate is interpolated onto the SAMI3 grid in magnetic coordinates. This is the heating rate that will be applied to electrons in the ‘CIMI heat’ simulation presented below. Figure 2(b) shows that CIMI-simulated Coulomb collisions between ring current ions and cold electrons occur at ionosphere altitudes, but only during the peak of the storm. Specifically panel (b) occurs during the first peak of the storm, marked by the second dashed vertical line in Figure 1(h). Additional plots, not shown, verify that direct heating of the ionosphere also occurs during the main peak of the storm (Day 280, 2300 UT). That is, CIMI model ring current ions lose energy to background electrons at ionosphere heights.

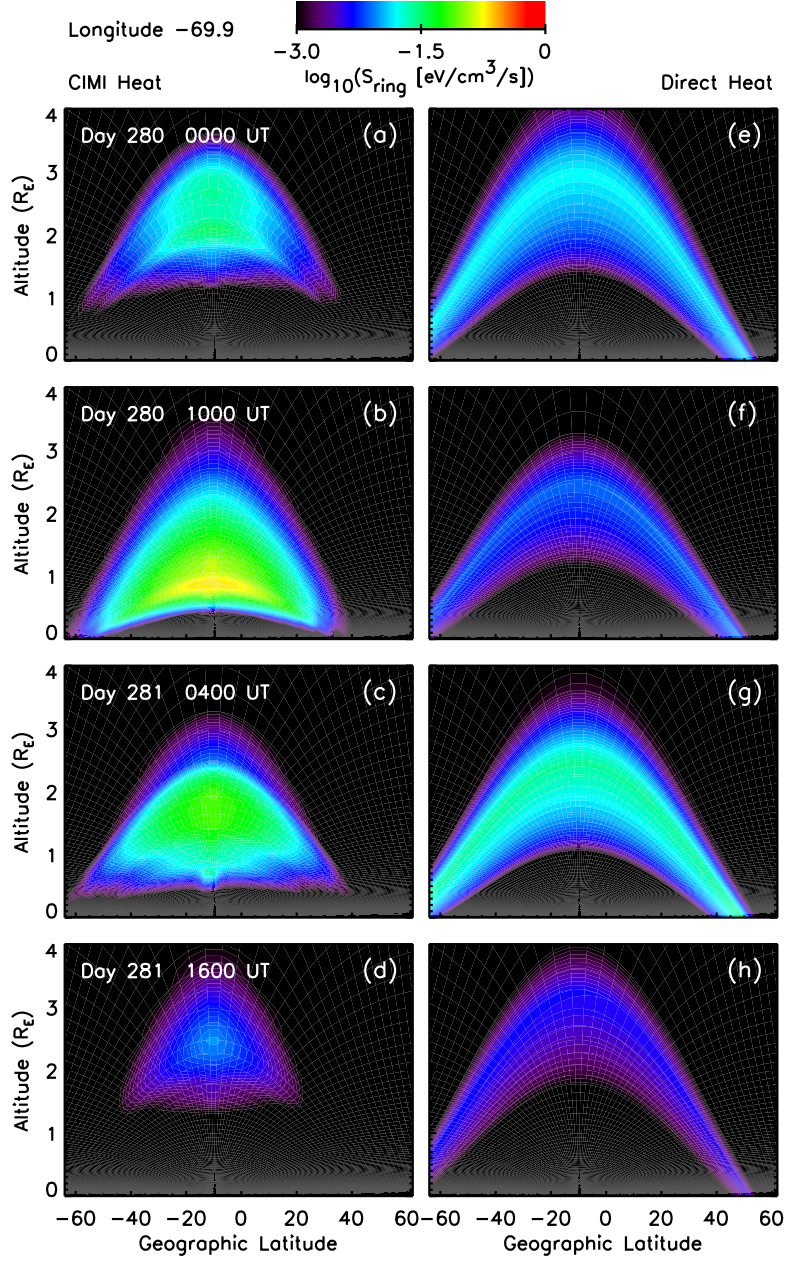


**Figure 2.** The log of the heating rate for ionosphere/plasmasphere electrons, caused by Coulomb collisions, plotted versus latitude and altitude at fixed longitude at four times. (a–d) show the heating rate simulated using CIMI. (e–h) show the model heating function specified in Krall et al. (2020), applied along each entire field line. SAMI3 simulations using these heating rates will be presented below.

### 3 SAMI3 modeling of the ionosphere and plasmasphere

The SAMI3 code was used to simulate the effect of ring current heating, via Coulomb collisions, of plasmasphere and ionosphere electrons. To test the hypothesis (Chappell, 1982; Horwitz et al., 1986; Roberts et al., 1987; R. H. Comfort et al., 1985) that ring current heating could generate the observed  $O^+$  shell, Krall et al. (2020) added a simple model ring current heating function to SAMI3. This heating model, a function only of the Dst index, was constructed such that the SAMI3 heating rate, when plotted in the equatorial plane, generally mimicked the field-line-averaged ring current energy loss rates computed by CIMI (see Figure 1 of Krall et al., 2020).

In Krall et al. (2020), the ring current heating function is incorrectly described as being “nonzero only above altitude  $1.7 R_E$ .” In fact, the heating was applied along the entire field line as shown in Figure 2(e–h). This, in part, prompted the present examination of the direct effect of the energy transferred from energetic ring current ions to the ionosphere via Coulomb collisions.

In this study we compare the ring current heating function of Krall et al. (2020) to the three-dimensional (3D) CIMI output and examine the effect of this heating on the ionosphere. We begin with Figure 1, a comparison of field-line-integrated heating from CIMI (panels a–c) to the field-line-integrated output from the model heating function (panels d–f). They are in reasonable quantitative agreement, with the CIMI heating being somewhat stronger than the model heating before the peak of the storm, and the model heating somewhat stronger after the peak of the storm. We next interpolated the 3D CIMI heating result, which was provided in magnetic coordinates, onto the SAMI3 grid. Because the SAMI3 grid is arranged with one dimension along the magnetic field (the other two dimensions are the field line index and the longitude), interpolation from CIMI to SAMI3 in magnetic coordinates was straightforward.

A comparison between the CIMI heating and the Dst-driven heating function is shown in Figure 2 for a fixed longitude (this same longitude will be used below to compare SAMI3 results to Millstone Hill observatory observations). The two are quite similar, except for panels (b) and (f), which are at the same time as Figure 1 (b, e).

#### 3.1 Direct heating of the ionosphere

Because CIMI-simulated ring current energy loss via Coulomb collisions with cold electrons occurs at all heights, it is reasonable to consider the effect, if any, of the direct heating of the ionosphere by ring current ions. Figure 3 shows the electron and ion temperatures at a specific location, magnetic latitude  $55^\circ$ , longitude  $70^\circ W$ , and altitude 500 km. Without heating (long dashed lines) a typical diurnal pattern is evident, with temperatures falling at night. With heating (all other curves), the diurnal pattern is affected because ring current heating is often strongest between late afternoon and midnight. Following the peak of the storm, at the beginning of day 281, the diurnal pattern is reversed, with a temperature maximum in the heated cases and a temperature minimum in the No Heat case.

Both the electron and ion temperatures increase during the storm, consistent with observations. For example, measurements at Millstone Hill (magnetic latitude  $54^\circ N$ , longitude  $71.5^\circ W$ ) by Pavlov and Buonsanto (1997, Fig. 6) and Liu et al. (2016, Fig. 7) show stormtime electron and ion temperature increases similar to those of Figure 3.

The heated cases, including the Indirect Heat case (dashed line), are all quite similar. This shows that simulated stormtime ionosphere temperature increases can be accounted for by heat conduction alone, without the direct heating effect that is present at all times in the Direct Heat case (solid line) and during the peak of the storm in the CIMI Heat case (dotted line). The Direct Heat case differs notably from the other cases

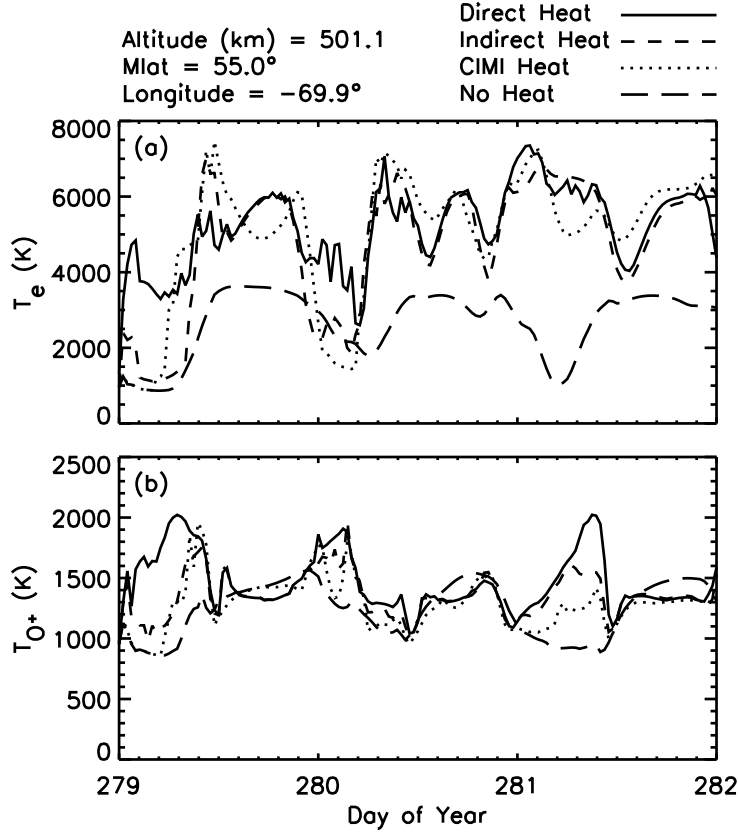


**Figure 3.** SAMI3 output showing (a) electron temperature and (b)  $O^+$  ion temperature for four cases: (solid curves) heating applied along entire field line as in Figure 2(e-h), (dashed curves) heating applied as in Figure 2(e-h), but only above altitude  $z > R_E/2$ , (dotted curves) CIMI heating as in Figure 2(a-d), and (long-dashed curves) no heating.



at the beginning of the simulation, early in day 279. At this time the Direct Heat case (solid line) has already obtained temperatures much higher than in the No Heat case (long-dashed line). In the  $T_e$  curves, this is repeated during the second diurnal minimum. Again,  $T_e$  in the Direct Heat case is elevated relative to the other three curves. Relative to the other curves, the Indirect Heat curve in Figure 3 is in closest agreement with the CIMI Heat curve. This suggests that the Dst-driven heating function in the Indirect Heat case is an improvement over that used in the Direct Heat case and in Krall et al. (2020).

### 3.2 Formation of the $O^+$ shell

Figure 4 shows the  $O^+$  shell in the equatorial plane at selected times for the Direct Heat case (a–c), the Indirect Heat case (d–f), and the CIMI Heat case (g–i). In each panel, a single contour line indicates plasmasphere electron density  $n_e = 100 \text{ cm}^{-3}$ . Figure 4(a–c), the Direct Heat case (see also Figure 1 d–f), has heating applied along the entire field line as shown in Figure 2(e–h). The panels in the center row, Figure 4(d–f), show the result for the Indirect Heat case, with heating limited to altitudes  $z > R_E/2$ , well above the topside ionosphere. The very close agreement between the top two rows of Figure 4 suggests that the direct heating of the ionosphere by ring current ions has little effect on the resulting  $O^+$  outflow. In the simulation using the CIMI heating rate interpolated onto the SAMI3 grid, Figure 4(g–i), we find results similar to the other cases in panels (g, h) and a stronger  $O^+$  shell later in the simulation (panel i). Consistent with the heating shown in Figure 2, the  $O^+$  shell in the CIMI Heat case has more structure than is seen in the other cases.

Because much of the data on the observed  $O^+$  shell comes from DE:RIMS (Dynamics Explorer: Retarding Ion Mass Spectrometer) profiles of ion composition versus radius (Chappell, 1982; Horwitz et al., 1984, 1986, 1990; Roberts et al., 1987; Fraser et al., 2005) or from measured electron and mass density profiles (Fraser et al., 2005; Grew et al., 2007; Takahashi et al., 2008; Nosé et al., 2011, 2015, 2018), we show corresponding SAMI3 profiles in Figure 5 for the case with CIMI-computed heating interpolated into the SAMI3 simulation. The profiles of Figure 5 can be directly compared to profiles at these same times and locations shown in Krall et al. (2020, Fig. 5) for a simulation using the model heating function of Figure 1(d–f) and Figure 2(e–h). The most notable difference relative to previous results is in the first column (Figure 5a,d,g), when the  $O^+$  radial profile has not yet distinguished itself from the  $H^+$  profile. Early in the storm, the  $O^+$  and  $N^+$  outflows appear to be simply adding mass to a typical plasmasphere profile. In other words, the model  $O^+$  density evolves from a plasmasphere-like structure to a shell-like structure. The degree to which this model result is present in observational data is not yet known.

In the second and third columns of Figure 5 we see the usual result: the average mass jumps at the plasmopause, correctly indicating a significant  $O^+$  component outside the plasmopause even as the bulk of the  $O^+$  shell is located inside the plasmopause.

## 4 Discussion

These SAMI3 results show that, while direct heating of the ionosphere is implied by CIMI simulations of ring current energy losses, the direct heating of the ionosphere by the ring current is not required to account for either the elevated ionosphere temperature during a storm or the  $O^+$  outflow that generates the  $O^+$  shell. However, many details of this process will need to wait until we have developed an improved coupling of the SAMI3 and CIMI models.



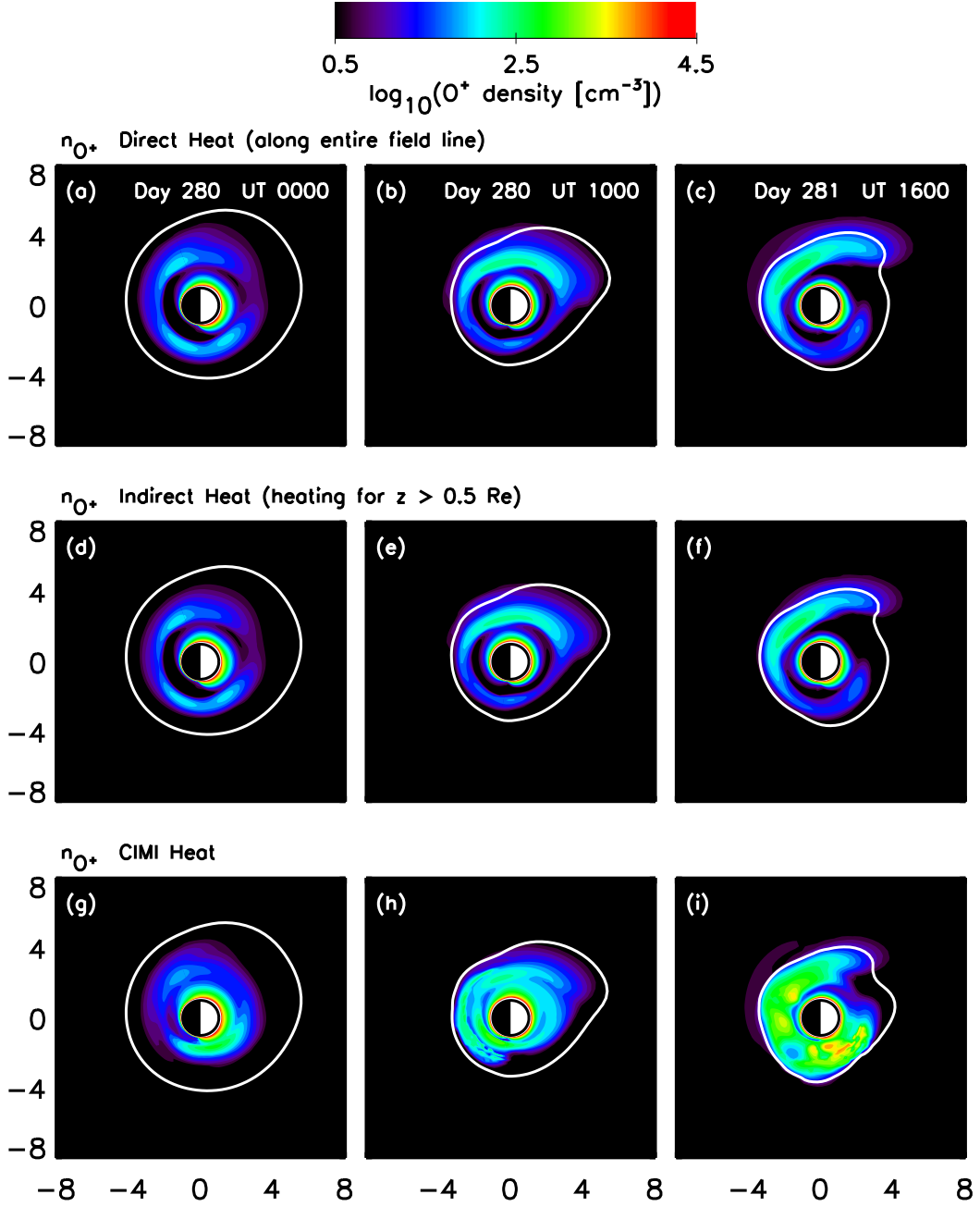


**Figure 4.** SAMI3 output showing  $\log_{10}n_{\text{O}^+}$  for (a–c) heating applied along the entire field line (Direct Heat), (d–f) heating applied only above altitude  $z > R_E/2$  (Indirect Heat), and (g–i) CIMI-computed heating interpolated into the SAMI3 simulation (CIMI Heat). Each column is at the same time as the corresponding column in Figure 1.

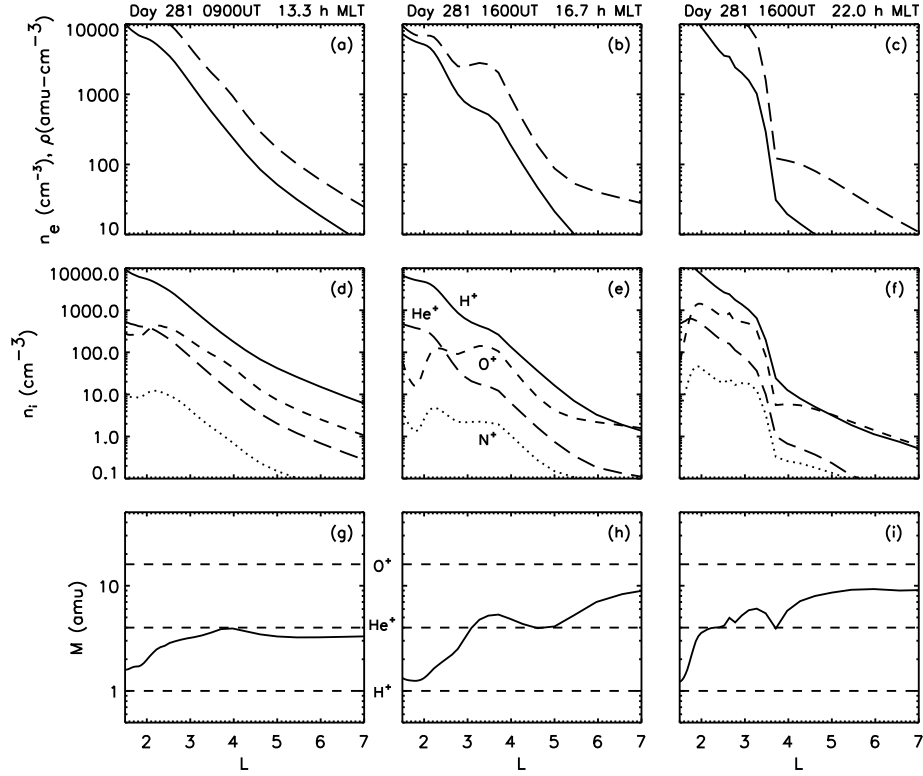


**Figure 5.** Radial profiles in the magnetic equatorial plane for the CIMI Heat case. Shown are (a–c) electron number density  $n_e$  (solid line) and ion mass density  $\rho$  (dashed line), (d–f) number density for  $H^+$ ,  $He^+$ ,  $N^+$  and  $O^+$  and (g–i) average mass density  $M$  (horizontal dashed lines indicate the  $H^+$ ,  $He^+$ , and  $O^+$  masses). Plots can be directly compared to those of Krall et al. (2020, Fig. 5), where the model heating function of Figure 1(d–f) and Figure 2(e–h), was used.

#### 207 4.1 Direct heating of the ionosphere

208 As shown in Figure 3, ring current heating affects the ionosphere temperature in  
 209 all cases where such heating was included. Early in day 281, the usual nighttime tem-  
 210 perature minimum is notably reversed. However, the general agreement among the three  
 211 heated cases shows that electron heat conduction plays a central role in these temper-  
 212 ature effects. These results are consistent with Liemohn et al. (2000), who used single-  
 213 field line modeling to show that ring current heating could account for elevated storm-  
 214 time ionosphere temperatures at Millstone Hill.

215 In one instance, the Direct Heat case deviates significantly from the other heated  
 216 cases. This occurs early in day 279, over 24 hours before the first peak of the storm, and  
 217 is evident in both panels of Figure 3. Here, the Indirect Heat, CIMI Heat, and No Heat  
 218 cases all agree on the nighttime temperature minimum (about 1000 K for both electrons  
 219 and ions) while the Direct Heat case shows elevated temperatures. These few hours of  
 220 the Direct Heat simulation contain the only clear signature of the direct heating of the  
 221 ionosphere and are, we suggest, not correct. For this reason, we find that the Dst-driven  
 222 heating function in the Indirect Heat case is an improvement over that used in Krall et  
 223 al. (2020). The CIMI simulation shows that direct heating of the ionosphere occurs only  
 224 during the peak of the storm, after heat conduction has already elevated the ionosphere  
 225 electron temperature relative to the No Heat case.

#### 226 4.2 Ionosphere/magnetosphere coupling

227 Relative to the SAMI3 simulation, where a Volland-Stern-Manyard/Chen magne-  
 228 topheric potential (Volland, 1973; Stern, 1975; Maynard & Chen, 1975; Reinisch et al.,  
 229 2009) was used, the CIMI simulation in Figure 1 shows a more strongly eroded plasma-  
 230 sphere (in both cases, the plasmasphere is indicated by a single contour line at  $n_e = 100$   
 231  $\text{cm}^{-3}$ ). This illustrates the challenge of coupling simulation codes. In this instance, for  
 232 example, SAMI3 lacks the CIMI magnetosphere potential while CIMI lacks the wind-  
 233 driven dynamo that has been shown to affect the shape of the plasmasphere (Krall et  
 234 al., 2014). The mismatch between the CIMI and SAMI3 magnetospheres might be af-  
 235 fecting the position of the heating (the energy lost by the ring current to the CIMI plas-  
 236 masphere) relative to the SAMI3 plasmopause. In our previous study, however, we found  
 237 that results were not sensitive to the position of the plasmopause.

238 As a further check on our results, we note that SAMI3 uses the apex coordinate  
 239 model (Richmond, 1995) for the geomagnetic field while CIMI uses an aligned dipole (low  
 240 altitude) plus the Tsyganenko and Sitnov (2005) model (higher altitudes). Because the  
 241 CIMI outputs the heating as a function of longitude, magnetic local time, and magnetic  
 242 field, the differing field models affect the interpolation of CIMI output into SAMI3. The  
 243 significance of this was tested by repeating the interpolation using a dipole model in SAMI3.  
 244 Again, the results were not sensitive to model specifics. Nevertheless, until an improved  
 245 SAMI3/CIMI simulation is shown to agree with measurements of the  $\text{O}^+$  shell for a spe-  
 246 cific event, many of these results must be considered provisional.

#### 247 4.3 Nitrogen ions

248 As can be seen in Figure 5, simulated  $\text{N}^+$  and  $\text{O}^+$  ion populations behave similarly,  
 249 with an  $\text{N}^+/\text{O}^+$  density ratio of a few percent. The similarity of  $\text{O}^+$  and  $\text{N}^+$  dynamics  
 250 in these simulations was further examined in a recent study (Krall & Huba, 2021, Fig.  
 251 5), where  $\text{O}^+$  and  $\text{N}^+$  field-aligned outflow velocities were found to be nearly identical.  
 252 The agreement between these results and DE-RIMS measurements of  $\text{N}^+$  in the  $\text{O}^+$  shell  
 253 (Chappell et al., 1982; Roberts et al., 1987) is significant because the  $n_{\text{N}^+}/n_{\text{O}^+}$  ratio is  
 254 an indicator of the energization mechanism that drives  $\text{O}^+$  and  $\text{N}^+$  outflows (Ilie & Liemohn,  
 255 2016). For example, Hoffman et al. (1974) finds that stormtime  $n_{\text{N}^+}/n_{\text{O}^+}$  often exceeds

unity, but only at high latitudes (above  $55^\circ$ ), where a variety of ion energization mechanisms can occur (Lin et al., 2020). The present qualitative agreement between these simulations and data supports the hypothesis that a relatively simple thermal heating mechanism produces both of these populations that make up the ‘heavy ion’ (Roberts et al., 1987; Fraser et al., 2005) shell.

## 5 Conclusion

This work further examines the hypothesis that Coulomb heating of plasmasphere electrons generates the cold stormtime  $O^+$  population in the inner magnetosphere known as the  $O^+$  torus or  $O^+$  shell. The consistent  $N^+/O^+$  density ratio of 0.05-0.2 in both the simulated outflow and in the DE:RIMS observations suggests that we have identified the correct type of energization process. Other ion energization processes, such as wave-particle interactions in polar regions, often generate much larger values of  $n_{N^+}/n_{O^+}$ . If the  $n_{N^+}/n_{O^+}$  ratio was better understood, and more commonly measured, it could aid in the identification of the energization process for any given observed  $O^+$  or  $N^+$  outflow (Ilie & Liemohn, 2016).

CIMI simulations show that ring current heating of ionosphere and plasmasphere electrons occurs at altitudes as low as 100 km. SAMI3 simulations show that, while energy is deposited along the entirety of a field line in many instances, affecting both the ionosphere and plasmasphere, the direct heating of the ionosphere by the ring current has only a minor impact on elevated stormtime ionosphere electron and ion temperatures, subsequent cold  $O^+$  outflows, and the resulting  $O^+$  shell. Direct heating of the ionosphere occurs only during the peaks of the storm, after the ionosphere electron temperature has already been elevated via electron heat conduction.

The present study further supports the hypothesis that the  $O^+$  shell is a result of direct thermal outflow from the ionosphere to the inner magnetosphere. These results are consistent with the DE:RIMS analysis of Horwitz et al. (1986), where ‘ring current coupling’ is suggested as ‘the most plausible explanation’ for elevated electron temperatures observed in the outer plasmasphere, and Horwitz et al. (1990), where elevated  $O^+$  density is found to correlate with elevated  $T_e$  rather than with the relative  $O^+$  density in the underlying ionosphere. However, improved coupling of the SAMI3 and CIMI models will be needed to reasonably verify these results. Specifically, we look forward to when we are able to directly compare results from a coupled SAMI3/CIMI model to further observations of these populations in the inner magnetosphere for one or more specific events.

## Acknowledgments

This research was supported by NRL Base Funds, NASA Grand Challenge award NNH17AE97I, and NASA Living With a Star award 80NSSC19K0089. Numerical information associated with each CIMI and SAMI3 figure, is available at <https://doi.org/10.5281/zenodo.6048640>. The heating function used in the Direct Heat case can be downloaded as FORTRAN code from <https://doi.org/10.5281/zenodo.3834161>.

## References

- Burch, J. L., Mitchell, D. G., Sandel, B. R., Brandt, P. C., & Wüest, M. (2001). Global dynamics of the plasmasphere and ring current during magnetic storms. *Geophysical Research Letters*, 28(6), 1159–1162. doi: 10.1029/2000GL012413
- Buzulukova, N., Fok, M.-C., Goldstein, J., Valek, P., McComas, D. J., & Brandt, P. C. (2010). Ring current dynamics in moderate and strong storms: Comparative analysis of TWINS and IMAGE/HENA data with the Comprehensive Ring Current Model. *Journal of Geophysical Research: Space Physics*,

- 115(A12). doi: 10.1029/2010JA015292
- Chappell, C. R. (1982). Initial observations of thermal plasma composition and energetics from Dynamics Explorer-1. *Geophysical Research Letters*, 9(9), 929–932. doi: 10.1029/GL009i009p00929
- Chappell, C. R., Olsen, R. C., Johnson, J. F. E., & Waite Jr., J. H. (1982). The discovery of nitrogen ions in the Earth’s magnetosphere. *Geophysical Research Letters*, 9(9), 937–940. doi: 10.1029/GL009i009p00937
- Cole, K. D. (1965). Stable auroral red arcs, sinks for energy of Dst main phase. *Journal of Geophysical Research*, 70(7), 1689–1706. doi: 10.1029/JZ070i007p01689
- Comfort, R. (1996). Thermal structure of the plasmasphere. *Advances in Space Research*, 17(10), 175–184. doi: 10.1016/0273-1177(95)00710-V
- Comfort, R. H., Waite Jr., J. H., & Chappell, C. R. (1985). Thermal ion temperatures from the retarding ion mass spectrometer on DE 1. *Journal of Geophysical Research: Space Physics*, 90(A4), 3475–3486. doi: 10.1029/JA090iA04p03475
- Fok, M.-C., Buzulukova, N. Y., Chen, S.-H., Glocer, A., Nagai, T., Valek, P., & Perez, J. D. (2014). The Comprehensive Inner Magnetosphere-Ionosphere model. *Journal of Geophysical Research: Space Physics*, 119(9), 7522–7540. doi: 10.1002/2014JA020239
- Fok, M.-C., Craven, P. D., Moore, T. E., & Richards, P. G. (1995). Ring current-plasmasphere coupling through Coulomb collisions. In *Cross-scale coupling in space plasmas* (pp. 161–171). American Geophysical Union (AGU). doi: 10.1029/GM093p0161
- Fok, M. C., Kozyra, J. U., Nagy, A. F., Rasmussen, C. E., & Khazanov, G. V. (1993). Decay of equatorial ring current ions and associated aeronomical consequences. *Journal of Geophysical Research: Space Physics*, 98(A11), 19381–19393. doi: 10.1029/93JA01848
- Fok, M.-C., Wolf, R. A., Spiro, R. W., & Moore, T. E. (2001). Comprehensive computational model of Earth’s ring current. *Journal of Geophysical Research: Space Physics*, 106(A5), 8417–8424. doi: 10.1029/2000JA000235
- Fraser, B. J., Horwitz, J. L., Slavin, J. A., Dent, Z. C., & Mann, I. R. (2005). Heavy ion mass loading of the geomagnetic field near the plasmopause and ULF wave implications. *Geophysical Research Letters*, 32(4). doi: 10.1029/2004GL021315
- Grew, R. S., Menk, F. W., Clilverd, M. A., & Sandel, B. R. (2007). Mass and electron densities in the inner magnetosphere during a prolonged disturbed interval. *Geophysical Research Letters*, 34(2). doi: 10.1029/2006GL028254
- Gringauz, K. I. (1983). Plasmasphere and its interaction with the ring current. *Space Sci. Rev.*, 34, 245–257. doi: 10.1007/BF00175281
- Gurgiolo, C., Sandel, B. R., Perez, J. D., Mitchell, D. G., Pollock, C. J., & Larsen, B. A. (2005). Overlap of the plasmasphere and ring current: Relation to sub-auroral ionospheric heating. *Journal of Geophysical Research: Space Physics*, 110(A12). doi: 10.1029/2004JA010986
- Hoffman, J. H., Dodson, W. H., Lippincott, C. R., & Hammack, H. D. (1974). Initial ion composition results from the Isis 2 satellite. *Journal of Geophysical Research (1896-1977)*, 79(28), 4246–4251. doi: 10.1029/JA079i028p04246
- Horwitz, J. L., Brace, L. H., Comfort, R. H., & Chappell, C. R. (1986). Dual-spacecraft measurements of plasmasphere-ionosphere coupling. *Journal of Geophysical Research: Space Physics*, 91(A10), 11203–11216. doi: 10.1029/JA091iA10p11203
- Horwitz, J. L., Comfort, R. H., & Chappell, C. R. (1984). Thermal ion composition measurements of the formation of the new outer plasmasphere and double plasmopause during storm recovery phase. *Geophysical Research Letters*, 11(8), 701–704. doi: 10.1029/GL011i008p00701

- Horwitz, J. L., Comfort, R. H., Richards, P. G., Chandler, M. O., Chappell, C. R., Anderson, P., ... Brace, L. H. (1990). Plasmasphere-ionosphere coupling: 2. ion composition measurements at plasmaspheric and ionospheric altitudes and comparison with modeling results. *Journal of Geophysical Research: Space Physics*, 95(A6), 7949–7959. doi: 10.1029/JA095iA06p07949
- Huba, J. D., Joyce, G., & Fedder, J. A. (2000). Sami2 is another model of the ionosphere (SAMI2): A new low-latitude ionosphere model. *Journal of Geophysical Research: Space Physics*, 105(A10), 23035–23053. doi: 10.1029/2000JA000035
- Huba, J. D., & Krall, J. (2013). Modeling the plasmasphere with SAMI3. *Geophysical Research Letters*, 40, 6–10. doi: 10.1029/2012GL054300
- Huba, J. D., Sazykin, S., & Coster, A. (2017). SAMI3-RCM simulation of the 17 March 2015 geomagnetic storm. *Journal of Geophysical Research: Space Physics*, 122(1), 1246–1257. doi: 10.1002/2016JA023341
- Ilie, R., & Liemohn, M. W. (2016). The outflow of ionospheric nitrogen ions: A possible tracer for the altitude-dependent transport and energization processes of ionospheric plasma. *Journal of Geophysical Research: Space Physics*, 121(9), 9250–9255. doi: 10.1002/2015JA022162
- Kozyra, J. U., Nagy, A. F., & Slater, D. W. (1997). High-altitude energy source(s) for stable auroral red arcs. *Reviews of Geophysics*, 35(2), 155–190. doi: 10.1029/96RG03194
- Krall, J., & Huba, J. D. (2021). Counterstreaming cold  $H^+$ ,  $He^+$ ,  $O^+$ , and  $N^+$  outflows in the plasmasphere. *Frontiers in Astronomy and Space Sciences*, 8, 712611. doi: 10.3389/fspas.2021.712611
- Krall, J., Huba, J. D., Denton, R. E., Crowley, G., & Wu, T.-W. (2014). The effect of the thermosphere on quiet time plasmasphere morphology. *Journal of Geophysical Research: Space Physics*, 119(6), 5032–5048. doi: 10.1002/2014JA019850
- Krall, J., Huba, J. D., & Fok, M.-C. (2020). Does ring current heating generate the observed  $O^+$  shell? *Geophysical Research Letters*, 47(14), e2020GL088419. doi: 10.1029/2020GL088419
- Liemohn, M. W., Kozyra, J. U., Richards, P. G., Khazanov, G. V., Buonsanto, M. J., & Jordanova, V. K. (2000). Ring current heating of the thermal electrons at solar maximum. *Journal of Geophysical Research: Space Physics*, 105(A12), 27767–27776. doi: 10.1029/2000JA000088
- Lin, M.-Y., Ilie, R., & Gloer, A. (2020). The contribution of  $N^+$  ions to Earth’s polar wind. *Geophysical Research Letters*, 47(18), e2020GL089321. doi: 10.1029/2020GL089321
- Liu, J., Wang, W., Burns, A., Yue, X., Zhang, S., Zhang, Y., & Huang, C. (2016). Profiles of ionospheric storm-enhanced density during the 17 March 2015 great storm. *Journal of Geophysical Research: Space Physics*, 121(1), 727–744. doi: 10.1002/2015JA021832
- Maynard, N. C., & Chen, A. J. (1975). Isolated cold plasma regions: Observations and their relation to possible production mechanisms. *Journal of Geophysical Research*, 80(7), 1009–1013. doi: 10.1029/JA080i007p01009
- McIlwain, C. E. (1961). Coordinates for mapping the distribution of magnetically trapped particles. *Journal of Geophysical Research*, 66(11), 3681–3691. doi: 10.1029/JZ066i011p03681
- Nosé, M., Matsuoka, A., Kumamoto, A., Kasahara, Y., Goldstein, J., Teramoto, M., ... MacDowall, R. J. (2018). Longitudinal structure of oxygen torus in the inner magnetosphere: Simultaneous observations by Arase and Van Allen Probe A. *Geophysical Research Letters*, 45(19), 10,177–10,184. doi: 10.1029/2018GL080122
- Nosé, M., Oimatsu, S., Keika, K., Kletzing, C. A., Kurth, W. S., Pascuale, S. D., ... Larsen, B. A. (2015). Formation of the oxygen torus in the inner magne-

- 414        atmosphere: Van Allen Probes observations.     *Journal of Geophysical Research:*  
415        *Space Physics*, 120(2), 1182–1196. doi: 10.1002/2014JA020593
- 416    Nosé, M., Takahashi, K., Anderson, R. R., & Singer, H. J. (2011). Oxygen torus in  
417        the deep inner magnetosphere and its contribution to recurrent process of O<sup>+</sup>-  
418        rich ring current formation.     *Journal of Geophysical Research: Space Physics*,  
419        116(A10). doi: 10.1029/2011JA016651
- 420    Ober, D. M., Horwitz, J. L., & Gallagher, D. L. (1997). Formation of density  
421        troughs embedded in the outer plasmasphere by subauroral ion drift events.  
422        *Journal of Geophysical Research: Space Physics*, 102(A7), 14595–14602. doi:  
423        10.1029/97JA01046
- 424    Pavlov, A. V., & Buonsanto, M. J. (1997). Comparison of model electron densities  
425        and temperatures with Millstone Hill observations during undisturbed periods  
426        and the geomagnetic storms of 16-23 March and 6-12 April 1990.     *Annales*  
427        *Geophysicae*, 15(3), 327–344. doi: 10.1007/s00585-997-0327-4
- 428    Reinisch, B. W., Moldwin, M. B., Denton, R. E., Gallagher, D. L., Matsui, H., Pier-  
429        rard, V., & Tu, J. (2009). Augmented empirical models of plasmaspheric  
430        density and electric field using IMAGE and CLUSTER data.     *Space Sci. Rev.*,  
431        145, 1231–1261. doi: 10.1007/s11214-008-9481-6
- 432    Richmond, A. D. (1995). Ionospheric electrodynamics using magnetic apex coor-  
433        dinate.     *Journal of geomagnetism and geoelectricity*, 47(2), 191–212. doi: 10  
434        .5636/jgg.47.191
- 435    Roberts, W. T., Horwitz, J. L., Comfort, R. H., Chappell, C. R., Waite Jr., J. H., &  
436        Green, J. L. (1987). Heavy ion density enhancements in the outer plasmas-  
437        phere.     *Journal of Geophysical Research: Space Physics*, 92(A12), 13499–13512.  
438        doi: 10.1029/JA092iA12p13499
- 439    Stern, D. P. (1975). The motion of a proton in the equatorial magnetosphere.     *Jour-*  
440        *nal of Geophysical Research*, 80(4), 595–599. doi: 10.1029/JA080i004p00595
- 441    Takahashi, K., Ohtani, S.-i., Denton, R. E., Hughes, W. J., & Anderson, R. R.  
442        (2008). Ion composition in the plasma trough and plasma plume derived  
443        from a Combined Release and Radiation Effects Satellite magnetoseismic  
444        study.     *Journal of Geophysical Research: Space Physics*, 113(A12). doi:  
445        10.1029/2008JA013248
- 446    Tsyganenko, N. A., & Sitnov, M. I. (2005). Modeling the dynamics of the inner  
447        magnetosphere during strong geomagnetic storms.     *Journal of Geophysical Re-*  
448        *search: Space Physics*, 110(A3). doi: 10.1029/2004JA010798
- 449    Volland, H. (1973). A semiempirical model of large-scale magnetospheric  
450        electric fields.     *Journal of Geophysical Research*, 78(1), 171–180. doi:  
451        10.1029/JA078i001p00171